Geophysical Research Letters

RESEARCH LETTER
10.1029/2021GL092982

Key Points:

- In eddy-rich ocean frontal regions, Ekman pumping can account for 10%–20% of vertical eddy heat flux at 50 m depth
- Eddy current feedback on wind stress is the key mechanism for Ekman pumping induced vertical eddy heat flux
- The results of this work suggest the wind-forced vertical eddy heat transport should be considered in the submesoscale parameterization

Supporting Information:

Supporting Information may be found in the online version of this article.

Correspondence to:

D. Li,
dapengli@tamu.edu

Citation:

Li, D., Chang, P., Ramachandran, S., Jing, Z., Zhang, Q., Kurian, J., et al. (2021). Contribution of the two types of Ekman pumping induced eddy heat flux to the total vertical eddy heat flux. *Geophysical Research Letters*, *48*, e2021GL092982. https://doi.org/10.1029/2021GL092982

Received 22 FEB 2021
Accepted 26 APR 2021

Contribution of the Two Types of Ekman Pumping Induced Eddy Heat Flux to the Total Vertical Eddy Heat Flux

Dapeng Li[1,2], Ping Chang[1,2,3], Sanjiv Ramachandran[1,2], Zhao Jing[1,4], Qiuying Zhang[1,2], Jaison Kurian[1,2], Abishek Gopal[1,2], and Haiyuan Yang[1,4]

[1]International Laboratory for High-Resolution Earth System Prediction, Texas A&M University, College Station, TX, USA, [2]Department of Oceanography, Texas A&M University, College Station, TX, USA, [3]Department of Atmospheric Sciences, Texas A&M University, College Station, TX, USA, [4]Key Laboratory of Physical Oceanography/Institute for Advanced Ocean Studies, Ocean University of China and Qingdao National Laboratory for Marine Science and Technology, Qingdao, China

Abstract Based on eddy-rich (0.1° horizontal resolution for ocean) Community Earth System Model simulations, we compute the Ekman pumping induced vertical eddy heat flux using two formulations: the classical and the Stern-Ekman pumping. The two mechanisms yield similar patterns in the eddy-induced vertical heat flux, showing strong upward heat flux in ocean frontal regions such as the western boundary current regions. Using the Gulf Stream Extension region as an example, we estimate (1) the Stern-Ekman pumping induced eddy heat flux is 23% and 12% of the total vertical eddy heat flux at 50 m depth during summer and winter, respectively; (2) the classical Ekman pumping accounts for 82% and 88% of the Stern-Ekman pumping induced eddy heat flux at 50 m during summer and winter, respectively. The second finding indicates eddy current feedback on wind stress is the primary cause for the upward eddy heat flux generated by Ekman pumping.

Plain Language Summary The classical Ekman pumping is well-known for its role in driving global ocean circulations. Stern-Ekman pumping modifies the classical Ekman pumping by taking into consideration of ocean eddy vorticity. In this study, we investigate the Ekman pumping induced eddy vertical heat flux using the two formulations above. Based on an eddy-rich climate model simulation, we find the eddy heat flux induced by the Stern-Ekman pumping can account for ~10%–20% the total vertical eddy heat flux at 50 m in eddy-rich ocean frontal regions, such as the Antarctic circumpolar region and the subtropical western boundary current regions. Comparison of the two Ekman pumping formulations shows the classical Ekman pumping can account for the majority of the Stern-Ekman pumping induced eddy heat flux, although the classical Ekman pumping generates much weaker vertical motions than the Stern-Ekman pumping. The results of this work suggest that parameterizing vertical eddy heat flux within the upper ocean mixed layer should take into consideration of the wind-forced eddy heat flux component.

1. Introduction

Ekman pumping refers to the vertical motions induced by winds (Ekman, 1905). The classical Ekman pumping theory predicts the Ekman pumping velocity is determined by the surface wind stress and the Coriolis parameter (Risien & Chelton, 2008). Stern (1965) demonstrated that the geostrophic vorticity also affects the vertical Ekman pumping and developed an expression for the Ekman pumping velocity that accounts for the effects of geostrophic vorticity from ocean eddies (hereafter referred to as the Stern-Ekman pumping velocity). The classical and the Stern-Ekman pumping generate different vertical motions within ocean eddies. For the classical Ekman pumping, upward or downward vertical velocity occurs near the center of an eddy due to eddy current feedback on surface wind stress (Klein & Lapeyre, 2009; Martin & Richards, 2001). The presence of ocean eddy currents causes an additional wind stress curl over eddies, which induces upward or downward vertical velocity near the center of eddies (Figure S1). For the Stern-Ekman pumping, Gaube et al. (2015) analyzed eddy composites based on satellite observations and found upward and downward vertical velocities on the opposite flanks of eddies. In addition to different velocity structures, the Stern-Ekman pumping has been shown to produce much stronger vertical motions

than the classical Ekman pumping, particularly at submesoscales where eddy vorticity becomes very strong (Mahadevan et al., 2008).

Vertical heat transports are of great importance to climate systems (Griffies et al., 2015; Jing, Wang, et al., 2020; Siegelman et al., 2020; Wolfe et al., 2008). A variety of frontal processes in the upper ocean generate vertical heat flux with a shallow peak in the surface layer (McWilliams, 2016). By comparing climate simulations with different ocean model resolutions (1°, 0.25°, and 0.1° horizontal resolutions), Griffies et al. (2015) showed: (a) transient mesoscale eddies act to transport heat upwards in the ocean; (b) a near-surface peak in the transient eddy heat transport emerges as the ocean resolution increases from 1° to 0.1° grid spacing. Using Community Earth System Model (CESM) simulations with a 0.1° horizontal resolution for ocean, Jing, Wang, et al. (2020) found significant upward eddy heat flux with a peak at ∼50 m depth in the subtropical western boundary current regions. They suggested the large vertical eddy heat flux was mainly attributed to an ageostrophic secondary circulation that acts to restore vertical shear in the frontal region against destruction by turbulent mixing. Since the Ekman pumping can directly induce vertical motions within eddies (Gaube et al., 2015; McGillicuddy et al., 2008), here we examine the questions: To what extent can the Ekman pumping (both the classical and the Stern-Ekman pumping) contribute to the vertical eddy heat flux within the upper ocean mixed layer in eddy-rich ocean frontal regions?

The vertical heat transports driven by the Ekman pumping can be decomposed into a temporal mean flow and eddy driven component. The mean flow component acts to generate downward heat transports (Cummins et al., 2016; Griffies et al., 2015). However, to the best of our knowledge, the contribution to the total vertical eddy heat flux from the Ekman velocity has not been quantified in the literature. Motivated by the above discussion, the purpose of this work is to (a) compute and compare the vertical eddy heat flux induced by the classical and the Stern-Ekman pumping; (b) quantify the contributions of the Ekman pumping induced vertical eddy heat flux to the total vertical eddy heat flux. The data sets used in this work are from an eddy-rich (0.1° horizontal resolution for ocean) global CESM simulation. The study is structured as below: we describe the methodology in Section 2, summarize the results in Section 3, and present discussion and conclusions in Section 4.

2. Methodology

2.1. Model Description

The simulation used in this study is a 4-year extended run of a present-day climate simulation (year 2000 greenhouse gas conditions with a fixed CO_2 concentration of 367 ppm) using a high resolution configuration of the CESM (Hurrell et al., 2013) described by Small et al. (2014). This CESM configuration consists of the Community Atmospheric Model version 5 (CAM5, Neale et al., 2010) with a spectral element (SE) dynamical core at 0.25° horizontal resolution and 30 levels in the vertical and the Parallel Ocean Program version 2 (POP2, Smith et al., 2010) with a nominal horizontal resolution of 0.1° and 62 vertical layers. The vertical resolution in the upper 100 m of the ocean model is 10 m. CAM5 and POP2 communicate with a coupler every 10 min and 6 h, respectively (Small et al., 2014). The coupler collects sea surface temperature from ocean and provides the updated surface flux computed using the Large and Yeager (2009) scheme. More details about this high resolution CESM simulation can be found in Small et al. (2014). The 4-year extension of this simulation outputs daily mean model variables, including surface wind stress, sea surface height, ocean temperature and vertical velocity, which will be used in this study.

2.2. Classical and Stern-Ekman Pumping Vertical Velocities

The classical Ekman pumping velocity (W_{CE}) is computed as:

$$W_{CE} = \frac{1}{\rho_0} \nabla \times \frac{\boldsymbol{\tau}}{f}, \tag{1}$$

where $\rho_0 = 1{,}020\ \mathrm{kg/m^3}$ is the reference density of sea water, f is the Coriolis parameter, and $\boldsymbol{\tau}$ is the surface wind stress vector (Risien & Chelton, 2008). The surface wind stress is calculated as

$$\boldsymbol{\tau} = \rho_a C_D \left(\boldsymbol{U_a} - \boldsymbol{U_o}\right)\left|\boldsymbol{U_a} - \boldsymbol{U_o}\right|, \tag{2}$$

where ρ_a is the air density, C_D is the drag coefficient, $\boldsymbol{U_o}$ and $\boldsymbol{U_a}$ are the vector velocities for ocean and atmosphere, respectively. The presence of ocean eddy currents, $\boldsymbol{U_o}$, modifies surface wind stress and affects W_{CE} over eddies (e.g., Martin & Richards, 2001). We emphasize that even though atmospheric process has large spatial scales, W_{CE} can have ocean eddy scales because of the eddy current feedback on wind stress in Equation 2 (Renault et al., 2017). We will demonstrate later that this influence of ocean eddies on W_{CE} accounts for the majority the Stern-Ekman pumping induced vertical eddy heat flux.

Stern (1965) formulated the Ekman pumping velocity (W_{SE}) associated with geostrophic vorticity from ocean eddies using:

$$W_{SE} = \frac{1}{\rho_0}\nabla \times \frac{\boldsymbol{\tau}}{f + \xi_g}, \tag{3}$$

$$\xi_g = \frac{\partial v_g}{\partial x} - \frac{\partial u_g}{\partial y}, \tag{4}$$

$$u_g = -\frac{g}{f}\frac{\partial \eta}{\partial y}, \tag{5}$$

$$v_g = \frac{g}{f}\frac{\partial \eta}{\partial x}, \tag{6}$$

where ξ_g is the vertical component of the geostrophic vorticity vector, g is the acceleration due to gravity, η is the sea surface height, u_g and v_g are the geostrophic currents in zonal and meridional directions. W_{SE} is not defined if $f + \xi_g \approx 0$, namely, f and ξ_g are of opposite signs and of same amplitude. Stern (1965) proposed this Ekman pumping velocity assuming geostrophic Rossby number ($Ro_g = \frac{\xi_g}{f}$) is less than O(1). In eddy-rich ocean frontal regions such as Kuroshio and Gulf Stream Extension regions, Ro_g computed from the model outputs barely exceeds 0.5 (Figure S2). This enables us to apply the Stern-Ekman pumping in this study. Compared with Equations 1 and 3 shows the presence of ocean eddies affects W_{SE} in two ways through eddy current feedback on wind stresses (Equation 2) and modification of the local Coriolis parameter f by the geostrophic vorticity ξ_g from ocean eddies.

2.3. Vertical Eddy Heat Flux

Vertical heat transports in the ocean can be decomposed into contributions from the mean flow and eddies. The purpose of this work is to investigate the contributions of Ekman pumping velocity to the total vertical eddy heat flux. Thus, in the rest of this document, "vertical heat flux" refers to the flux generated by eddy fields.

The total vertical eddy heat flux (Q_{eddy}) is estimated as:

$$Q_{\text{eddy}}\left(x,y,z\right) = \rho_0 C_p \overline{W'\left(x,y,z,t\right)T'\left(x,y,z,t\right)}, \tag{7}$$

$$W'\left(x,y,z,t\right) = W\left(x,y,z,t\right) - \overline{W\left(x,y,z,t\right)}, \tag{8}$$

$$T'\left(x,y,z,t\right) = T\left(x,y,z,t\right) - \overline{T\left(x,y,z,t\right)}, \tag{9}$$

where C_p is the specific heat at constant pressure and the overbar denotes the time average over the summer or winter. The primed variables are deviations from the time average. Here we define boreal summer (austral winter) as April to September and boreal winter (austral summer) as October to March. Positive flux indicates upward heat transports.

Analogous to Q_{eddy}, vertical heat flux induced by the classical Ekman pumping (Q_{CE}) and the Stern-Ekman pumping (Q_{SE}) are estimated as:

$$Q_{CE}(x,y,z) = \rho_0 C_p \overline{W'_{CE}(x,y,t)T'(x,y,z,t)}, \tag{10}$$

$$Q_{SE}(x,y,z) = \rho_0 C_p \overline{W'_{SE}(x,y,t)T'(x,y,z,t)}, \tag{11}$$

Ekman pumping occurs at the bottom of the Ekman layer, commonly referred as the Ekman pumping depth. The Ekman pumping depth (D_e) can be parameterized as $D_e = \frac{4.3U_a}{\sqrt{\sin(|\theta|)}}$, where U_a is the wind speed and θ is the latitude (Pond & Pickard, 2013). At mid-latitude ($\theta = 45°$), D_e varies with wind speed and ranges from 26 to 102 m with wind speeds varying from 5 and 20 m/s. To show global patterns in the vertical eddy heat flux generated by the classical and the Stern-Ekman pumping, we use a constant Ekman pumping depth of 50 m (Cummins et al., 2016), and compute heat flux using Equations 10 and 11 with temperature at 50 m. Since the Ekman pumping depth varies with both wind speed and latitude, we also compute the Ekman pumping induced vertical heat flux using Equations 10 and 11 with temperature at different depths from 10 to 110 m.

2.4. Eddy Composites

To explore the spatial structures of Q_{CE} and Q_{SE} within eddies, we conduct eddy composites in the Gulf Stream Extension region during the four boreal winter seasons using the simulation results. We use an eddy identification and tracking algorithm developed by Kurian et al. (2011), which has been used in a number of previous studies (Jing, Chang, et al., 2019; Liang et al., 2012). We identify eddies with simulated daily sea level anomalies ranging from −1.5 to 1.5 m and eddy radii between 50 and 200 km. We choose these ranges by visually examining surface elevation anomaly contours in the Gulf Stream Extension region during winter seasons. Following Frenger et al. (2013), we first scale identified eddies by its radius and rotate them to align with the large-scale wind direction such that the winds are always westerly. The rotated eddies are then averaged in time to generate eddy composites.

3. Results

3.1. Global Distribution

Significant upward $Q_{\text{eddy}}^{50\,\text{m}}$ is noted in the eddy-rich ocean frontal regions such as the Antarctic circumpolar region and the subtropical western boundary current regions (Figures 1a and 1b). The mean $Q_{\text{eddy}}^{50\,\text{m}}$ increases from summer to winter, as is clearly seen in the Gulf Stream Extension region and the Kuroshio Extension region (Figures 1a and 1b).

The classical and the Stern-Ekman pumping produce vertical eddy heat flux that bears a striking qualitative similarity to $Q_{\text{eddy}}^{50\,\text{m}}$ in eddy-rich ocean frontal regions except for the weaker amplitude (Figures 1c–1f). $Q_{SE}^{50\,\text{m}}$ and $Q_{CE}^{50\,\text{m}}$ mostly transports heat upward except for the north Pacific Ocean (40°N-50°N) during boreal winter (Figures 1d and 1f). Comparison between $Q_{SE}^{50\,\text{m}}$ and $Q_{CE}^{50\,\text{m}}$ reveals features in $Q_{SE}^{50\,\text{m}}$ are spatially coherent with $Q_{CE}^{50\,\text{m}}$ for a spatial scale over O(100 km) (Figures 1c–1f). The difference between $Q_{SE}^{50\,\text{m}}$ and $Q_{CE}^{50\,\text{m}}$ shows smaller scales of variability (Figures 1g and 1h). To compare Q_{CE} and Q_{SE} and characterize the contributions of Q_{CE} and Q_{SE} to Q_{eddy}, we focus on the Gulf Stream Extension region as an example in the following sections. Analysis of another subtropical western boundary current region, the Kuroshio Extension region, shows similar results and is presented in the supporting information.

3.2. Gulf Stream Extension Region

Strong $Q_{\text{eddy}}^{50\,\text{m}}$ is noted in the Gulf Stream Extension region between 35°N-42°N and 55°W-75°W (indicated by the black box in Figure 2b). Averaging $Q_{\text{eddy}}^{50\,\text{m}}$ over this region yields a more than twofold increase (from 36.2 to 85.8 W/m^2) from summer to winter. Seasonal changes are also evident in vertical profiles (Figure 3). During summer season, Q_{eddy} increases with depth in the upper water column from 10 to 110 m (Figure 3a).

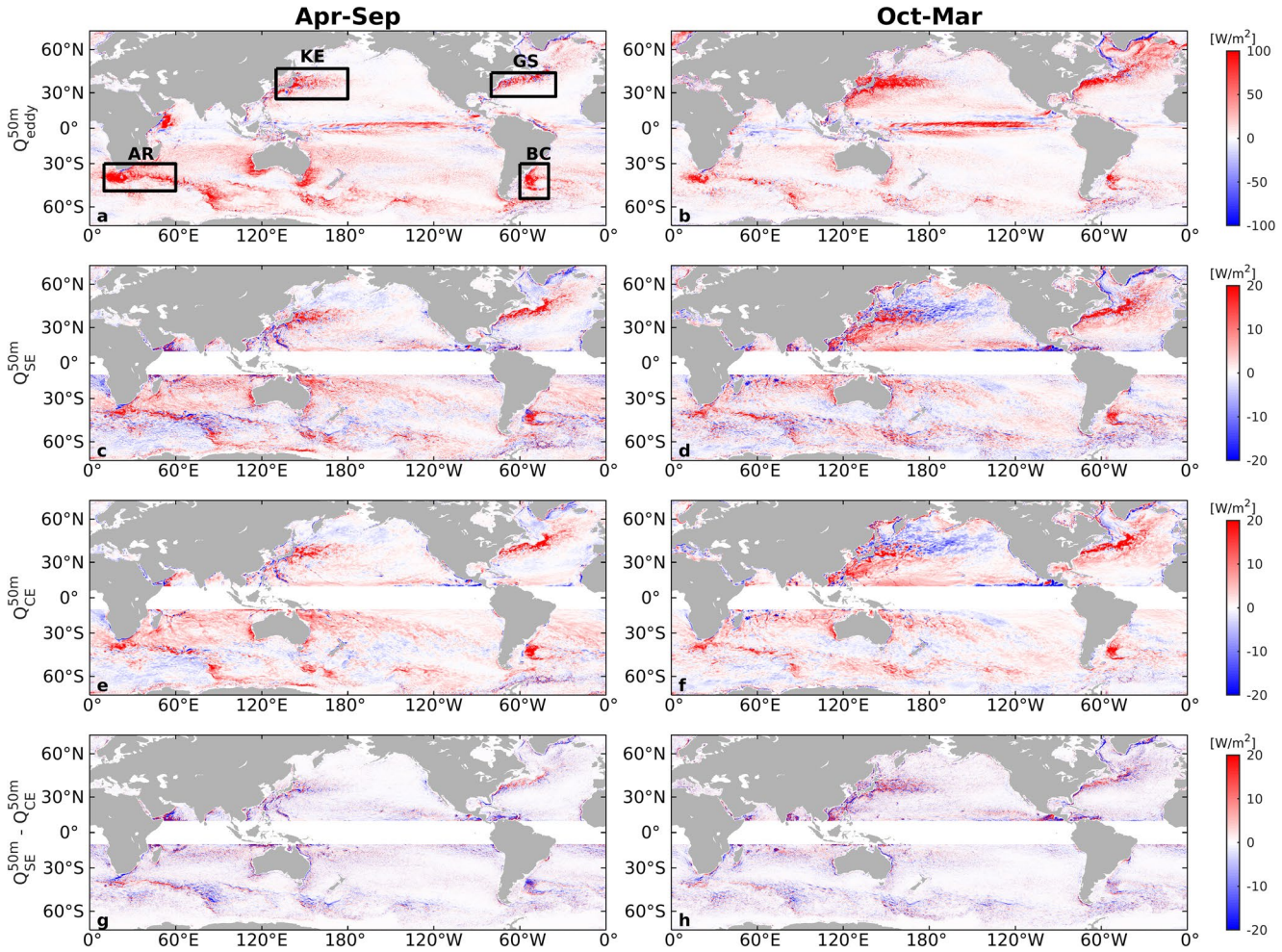

Figure 1. (a and b) Global distribution of total vertical eddy heat flux, (c and d) Stern-Ekman pumping induced vertical heat flux, (e and f) classical Ekman pumping induced vertical heat flux, and (g and h) the difference between the Stern and the classical Ekman pumping induced vertical heat flux during boreal summer (left column) and winter (right column). Superscript 50 m means the vertical heat flux is estimated at 50 m depth, see Section 2.3 for details. Different color ranges are used between the top panel and the rest due to different vertical heat flux ranges. Since the Ekman theory is not applicable near the equator where the Coriolis parameter vanishes, we do not show the results between 10°S and 10°N. Black boxes in (a) mark the four eddy-rich ocean frontal regions: Kuroshio Extension (KE) region, Gulf Stream (GS) Extension region, Agulhas Return (AR) current region, and Brazil Current (BC) region, where significant total vertical eddy heat flux is identified.

During winter season, Q_{eddy} first increases with depth and reaches a peak value close to 90 W/m^2 at 50 m, then gradually decreases toward 110 m depth (Figure 3b).

From summer to winter, the mean $Q_{SE}^{50\,\text{m}}$ (averaged over the black box region marked in Figure 2b) increases by 27% from 8.3 to 10.5 W/m^2 (Figures 2c and 2d). Within the same region, the spatially averaged $Q_{SE}^{50\,\text{m}}$ accounts for 23% and 12% of $Q_{\text{eddy}}^{50\,\text{m}}$ during summer and winter, respectively. Comparison of Q_{SE} at different depths shows a slight increase in Q_{SE} with depth compared to Q_{eddy} and at shallow depths (10–20 m) Q_{SE} is more comparable to Q_{eddy} (Figure 3).

Comparison between $Q_{SE}^{50\,\text{m}}$ and $Q_{CE}^{50\,\text{m}}$ shows $Q_{CE}^{50\,\text{m}}$ can account for the majority of $Q_{SE}^{50\,\text{m}}$ (Figures 2c–2h). During summer and winter seasons, the mean $Q_{CE}^{50\,\text{m}}$ is 6.8 and 9.2 W/m^2, accounting for 82% and 88% of the mean $Q_{SE}^{50\,\text{m}}$. Q_{CE} is generated by eddy current feedback on wind stress (Renault et al., 2017), while Q_{SE} is generated by both the eddy current feedback on wind stress and the modification of the local Coriolis parameter by eddy geostrophic vorticity (see Sections 2.2 and 2.3 for details). The consistency between Q_{CE} and Q_{SE} indicates the Stern-Ekman pumping induced vertical heat flux mainly results from the eddy current feedback on wind stress, which is further explained by the eddy composite analysis below.

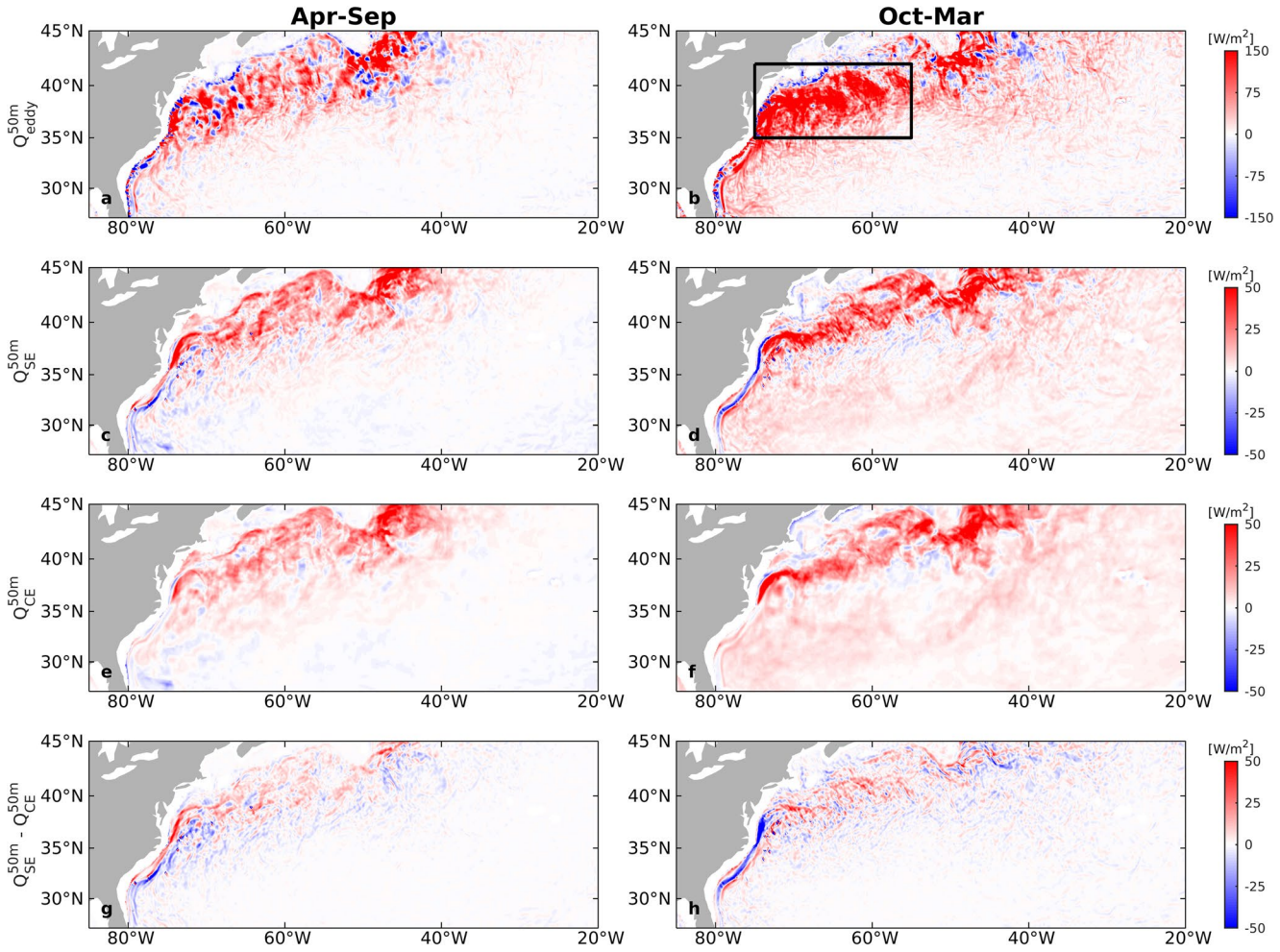

Figure 2. (a and b) Total vertical heat flux, (c and d) Stern-Ekman pumping induced vertical heat flux, (e and f) classical Ekman pumping induced vertical heat flux, and (g and h) the difference between the Stern and the classical Ekman pumping induced vertical heat flux at 50 m depth in the Gulf Stream Extension region during summer (left column) and winter (right column). Different color ranges are used between the top panel and the rest due to different vertical heat flux ranges. Black box in (b) marks the region (35°N-42°N, 55°W-75°W) of large total vertical eddy heat flux.

3.3. Eddy Composites of Ekman Pumping Induced Vertical Eddy Heat Flux

We conduct eddy composites in the Gulf Stream Extension region to show the spatial structures of $Q_{CE}^{50\,\mathrm{m}}$ and $Q_{SE}^{50\,\mathrm{m}}$ within eddies (Figure 4). Snapshots of 6,995 cyclonic eddies and 3,813 anti-cyclonic eddies are used to generate the eddy composites. Ekman pumping induced vertical heat flux in the eddy composites is estimated using temperature at 50 m depth.

For the classical Ekman pumping, downward and upward vertical velocities occur near the center of cyclonic and anti-cyclonic eddies, respectively (Figures 4a and 4c). For cyclonic and anti-cyclonic eddies, the presence of ocean eddy currents generates an additional negative and positive wind stress curl over eddies, respectively. The negative and positive wind stress curls induce downward and upward vertical velocities (Figure S1). The Stern-Ekman pumping produces dipole velocity structures in the opposite flanks of eddies (Figures 4b and 4d), consistent with Gaube et al. (2015). Both cyclonic and anti-cyclonic eddies induce positive $Q_{CE}^{50\,\mathrm{m}}$ (Figures 4e and 4g). For cyclonic eddies, negative W_{CE} and cold water temperature core generate upward heat transport (Figures 4a and 4e). For anti-cyclonic eddies, positive W_{CE} and warm water temperature core produce positive $Q_{CE}^{50\,\mathrm{m}}$ (Figures 4c and 4g).

$Q_{SE}^{50\,\mathrm{m}}$ shows dipole structures in cyclonic and anti-cyclonic eddies, with the positive and negative values occurring in the north and south sides of eddies (Figures 4f and 4h). For cyclonic eddies, the dipole patterns of

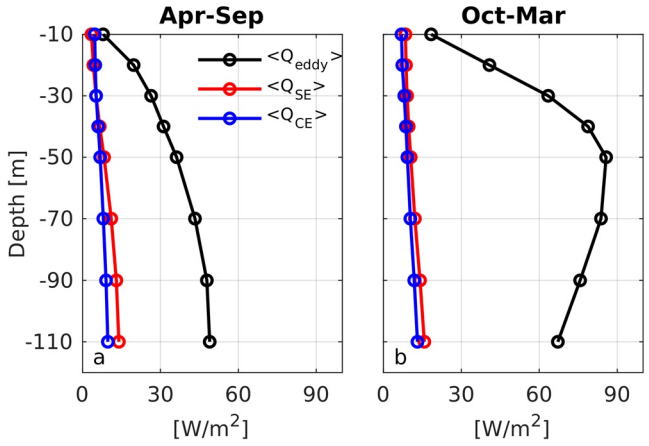

Figure 3. Total vertical eddy heat flux, the classical and the Stern-Ekman pumping induced vertical eddy heat flux during (a) summer and (b) winter. All vertical profiles are spatially averaged within the black box marked in Figure 2b, where large total vertical eddy heat flux is noted.

$Q_{SE}^{50\,\mathrm{m}}$ and W_{SE} are opposite due to the negative temperature anomaly within eddies. For anti-cyclonic eddies, the dipole patterns of $Q_{SE}^{50\,\mathrm{m}}$ and W_{SE} are the same due to the positive temperature anomaly within eddies. Although the amplitude of W_{SE} is stronger than W_{CE} (Figures 4a–4d), the magnitude of $Q_{SE}^{50\,\mathrm{m}}$ and $Q_{CE}^{50\,\mathrm{m}}$ are comparable (Figures 4e–4h). We attribute this to the spatial mismatch between W_{SE} and temperature anomalies. For cyclonic and anti-cyclonic eddies, the maximum temperature anomalies occur in the eddy center while W_{SE} reaches the maximum near the edge of eddies (Figures 4b and 4d). In addition, the dipole patterns of W_{SE} generate dipole patterns of $Q_{SE}^{50\,\mathrm{m}}$, which cancels each other in terms of the spatial averages (Figures 4b, 4d, 4f, and 4h). Thus, the large amplitudes of W_{SE} do not contribute much to the mean vertical heat flux and $Q_{CE}^{50\,\mathrm{m}}$ can account for the majority of $Q_{SE}^{50\,\mathrm{m}}$. This is consistent with the results shown in Section 3.2.

4. Discussion and Conclusions

Upward heat flux in the upper ocean can result from a range of frontal processes (McWilliams, 2016; Yang et al., 2021), some of which are parameterized in climate models (Fox-Kemper, Danabasoglu, et al., 2011). Unlike mesoscale baroclinic instability, these processes occur at lateral scales finer than O(100 km) and yield a peak in the vertical heat flux within the surface layer. In this study, we used a coupled, global eddy-rich (0.1° and 0.25° horizontal resolutions for ocean and atmosphere) CESM simulations to investigate the vertical eddy heat flux induced by one of these processes, namely, Ekman pumping, with an emphasis on the comparison between the classical and the Stern-Ekman pumping. Our analysis shows large classical and Stern-Ekman pumping induced upward eddy heat flux in the ocean frontal regions, such as the Antarctic circumpolar region and the subtropical western boundary current regions, bearing a strong

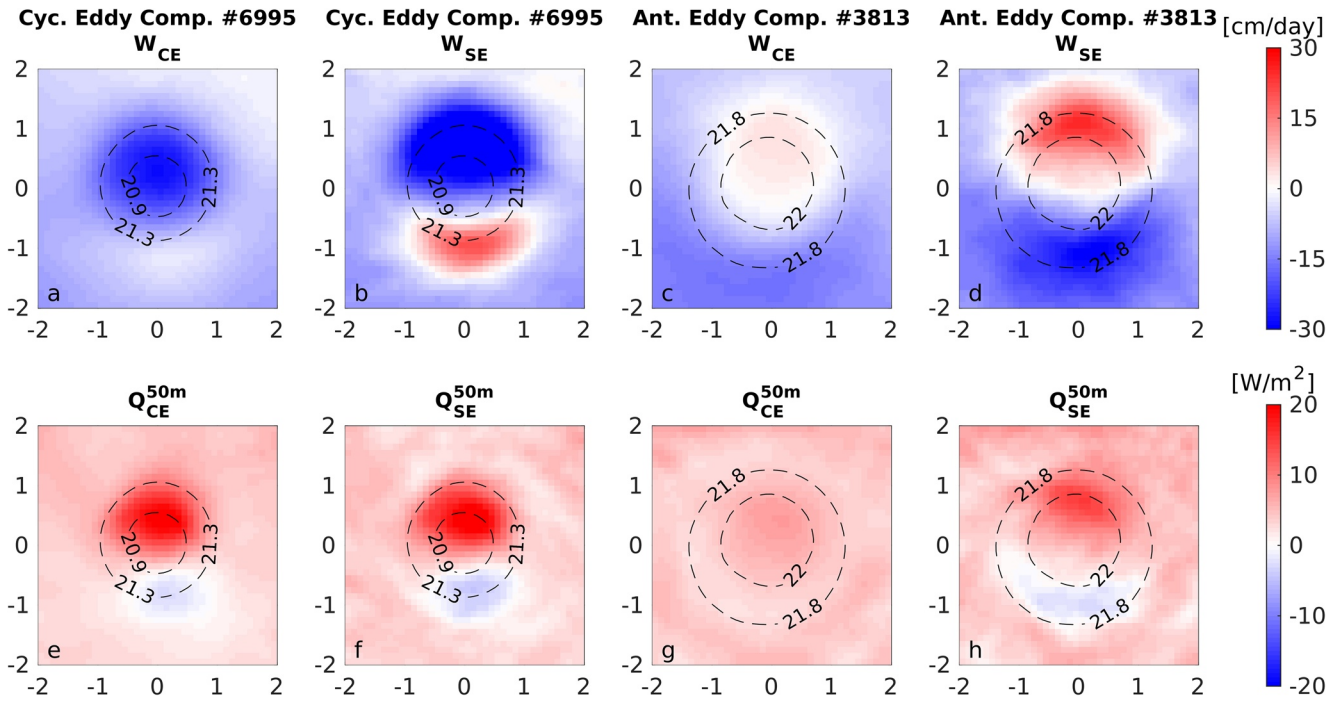

Figure 4. The first column shows the classical Ekman pumping velocity (a) and heat flux at 50 m depth (e) for cyclonic eddies. The second column shows the Stern-Ekman pumping velocity (b) and heat flux at 50 m depth (f) for cyclonic eddies. The third column shows the classical Ekman pumping velocity (c) and heat flux at 50 m depth (g) for anti-cyclonic eddies. The fourth column shows the Stern-Ekman pumping velocity (d) and heat flux at 50 m depth (h) for anti-cyclonic eddies. Black dashed contours show eddy composites of temperature at 50 m depth. The number of eddies used for composites are shown on the title at the top.

similarity to the total vertical eddy heat flux. In the Gulf Stream Extension region, the amplitude of vertical eddy flux is comparable to the total surface heat flux (Figure S7), consistent with Saenko (2015). Using the coupled CESM simulations, Jing, Wang, et al. (2020) found significant upward eddy heat flux in the subtropical western boundary current regions. They suggested the eddy vertical heat flux can be understood on the basis of turbulent thermal wind balance (Gula et al., 2014) and results primarily from restoring of vertical shear against destruction by turbulent mixing. Here we show that Ekman pumping in the presence of ocean eddies can also contribute to the total upward eddy heat flux in near-surface ocean. In the Gulf Stream Extension region, the area-averaged $Q_{SE}^{50\,\mathrm{m}}$ accounts for 23% and 12% of $Q_{\mathrm{eddy}}^{50\,\mathrm{m}}$ during summer and winter, respectively (Figures 2a–2d). It is interesting to note that the mean and eddy Ekman pumping velocities contribute differently to vertical heat transports. Through upwelling and downwelling, the mean Ekman flow brings cold middepth water upwards and warm surface water downwards. Thus, the mean Ekman flow acts to transport heat downwards (Cummins et al., 2016; Griffies et al., 2015). For the eddy-induced component, our results indicate it contributes to the upward eddy heat flux (Figures 1a–1d), consistent with the results shown by Morrison et al., (2013).

The classical Ekman pumping can account for the majority of the Stern-Ekman pumping induced vertical heat flux, although the two Ekman pumpings produce different velocity structures within eddies. The results of our eddy composite analysis show: (a) the classical Ekman pumping generates upward and downward vertical velocities near the center of anti-cyclonic and cyclonic eddies, respectively (Figures 4a and 4c); (b) the Stern-Ekman pumping produces dipole velocity structures within cyclonic and anti-cyclonic eddies (Figures 4b and 4d). The spatial patterns of W_{CE} and W_{SE} within eddies are consistent with previous studies (Gaube et al., 2015; Klein & Lapeyre, 2009; Martin & Richards, 2001). In addition, our results show comparable magnitudes of $Q_{SE}^{50\,\mathrm{m}}$ and $Q_{CE}^{50\,\mathrm{m}}$ within eddies (Figures 4e–4h), although the amplitude of W_{SE} is stronger than that of W_{CE} (Figures 4a–4d). We attribute this to the spatial mismatch between velocity and temperature anomalies. For both cyclonic and anti-cyclonic eddies, the maximum W_{SE} occurs near the edge of eddies, while temperature anomalies mainly reside in the eddy center (Figures 4b and 4d). In addition, the dipole patterns of W_{SE} produce upward and downward $Q_{SE}^{50\,\mathrm{m}}$, which cancel each other in terms of the spatial averages. Thus, the large amplitude of W_{SE} does not contribute to large vertical heat flux and the amplitudes of $Q_{SE}^{50\,\mathrm{m}}$ and $Q_{CE}^{50\,\mathrm{m}}$ are comparable. This is consistent with our results in Section 3.2. The consistency between $Q_{SE}^{50\,\mathrm{m}}$ and $Q_{CE}^{50\,\mathrm{m}}$ indicates eddy current feedback on wind stress produces the majority of the Stern-Ekman pumping induced heat flux.

Similar to the Ekman pumping, vertical heat flux generated by submesoscale process also occurs within mixed layer (Fox-Kemper & Ferrari, 2008; Su et al., 2018). Based on a submesoscale eddy resolving numerical simulation with a horizontal resolution of ~2 km, Su et al. (2018) showed significant near-surface upward heat flux in eddy-rich ocean frontal regions. During winter season, vertical eddy heat flux generated by the classical Ekman pumping are ~10% of the vertical eddy heat flux shown by Su et al. (2018). Fox-Kemper, Ferrari, and Hallberg (2008) developed a parameterization, based on baroclinic instability of submesoscale eddies and fronts within mixed layer, to incorporate submesoscale processes induced vertical buoyancy flux in climate models that do not explicitly resolve submesoscale eddies. Our results suggest the classical Ekman pumping contributes to the upward eddy heat flux in eddy-rich regions. Thus, future work may need to consider including the classical Ekman pumping induced eddy heat flux to the submesoscale parameterization.

Data Availability Statement

Data used for this study is accessible through https://datahub.geos.tamu.edu:8880/thredds/catalog/CESM_4yr_2021Feb19/catalog.html.

References

Cummins, P. F., Masson, D., & Saenko, O. A. (2016). Vertical heat flux in the ocean: Estimates from observations and from a coupled general circulation model. *Journal of Geophysical Research: Oceans*, *121*(6), 3790–3802. https://doi.org/10.1002/2016jc011647

Ekman, V. W. (1905). On the influence of the earth's rotation on ocean-currents. *Arkiv for Matematik, Astronomi och Fysik*, (2), 1–52.

Fox-Kemper, B., Danabasoglu, G., Ferrari, R., Griffies, S. M., Hallberg, R. W., Holland, M. M., et al. (2011). Parameterization of mixed layer eddies. III: Implementation and impact in global ocean climate simulations. *Ocean Modelling*, *39*(1–2), 61–78. https://doi.org/10.1016/j.ocemod.2010.09.002

Acknowledgments
This research is completed through the International Laboratory for High Resolution Earth System Prediction (iHESP)—a collaboration among the Qingdao National Laboratory for Marine Science and Technology (QNLM), Texas A&M University (TAMU), and the US National Center for Atmospheric Research (NCAR). P. Chang acknowledges the supports from National Science Foundation Grant AGS-1462127, Department of Energy Grant DE-SC0020072, and Department of Commence Grant NA20OAR4310409. Q. Zhang acknowledges the support from the China Scholarship Council. The authors thank the Texas A&M Supercomputing Facility and the Texas Advanced Computing Center (TACC) and NCAR-Wyoming Supercomputing Center for providing high performance computing resources that contributed to the research results reported in this study. The authors thank the anonymous reviewers for their insightful comments.

Fox-Kemper, B., & Ferrari, R. (2008). Parameterization of mixed layer eddies. Part II: Prognosis and impact. *Journal of Physical Oceanography*, *38*(6), 1166–1179. https://doi.org/10.1175/2007jpo3788.1

Fox-Kemper, B., Ferrari, R., & Hallberg, R. (2008). Parameterization of mixed layer eddies. Part I: Theory and diagnosis. *Journal of Physical Oceanography*, *38*(6), 1145–1165. https://doi.org/10.1175/2007jpo3792.1

Frenger, I., Gruber, N., Knutti, R., & Münnich, M. (2013). Imprint of Southern Ocean eddies on winds, clouds and rainfall. *Nature Geoscience*, *6*(8), 608–612. https://doi.org/10.1038/ngeo1863

Gaube, P., Chelton, D. B., Samelson, R. M., Schlax, M. G., & O'Neill, L. W. (2015). Satellite observations of mesoscale eddy-induced Ekman pumping. *Journal of Physical Oceanography*, *45*(1), 104–132. https://doi.org/10.1175/jpo-d-14-0032.1

Griffies, S. M., Winton, M., Anderson, W. G., Benson, R., Delworth, T. L., Dufour, C. O., et al. (2015). Impacts on ocean heat from transient mesoscale eddies in a hierarchy of climate models. *Journal of Climate*, *28*(3), 952–977. https://doi.org/10.1175/jcli-d-14-00353.1

Gula, J., Molemaker, M. J., & McWilliams, J. C. (2014). Submesoscale cold filaments in the Gulf Stream. *Journal of Physical Oceanography*, *44*(10), 2617–2643. https://doi.org/10.1175/jpo-d-14-0029.1

Hurrell, J. W., Holland, M. M., Gent, P. R., Ghan, S., Kay, J. E., Kushner, P. J., et al. (2013). The community earth system model: A framework for collaborative research. *Bulletin of the American Meteorological Society*, *94*(9), 1339–1360. https://doi.org/10.1175/bams-d-12-00121.1

Jing, Z., Chang, P., Shan, X., Wang, S., Wu, L., & Kurian, J. (2019). Mesoscale SST dynamics in the Kuroshio-Oyashio extension region. *Journal of Physical Oceanography*, *49*(5), 1339–1352. https://doi.org/10.1175/jpo-d-18-0159.1

Jing, Z., Wang, S., Wu, L., Chang, P., Zhang, Q., Sun, B., et al. (2020). Maintenance of mid-latitude oceanic fronts by mesoscale eddies. *Science Advances*, *6*(31), eaba7880. https://doi.org/10.1126/sciadv.aba7880

Klein, P., & Lapeyre, G. (2009). The oceanic vertical pump induced by mesoscale and submesoscale turbulence. *Annual Review of Marine Science*, *1*, 351–375. https://doi.org/10.1146/annurev.marine.010908.163704

Kurian, J., Colas, F., Capet, X., McWilliams, J. C., & Chelton, D. B. (2011). Eddy properties in the California current system. *Journal of Geophysical Research*, *116*(C8). https://doi.org/10.1029/2010jc006895

Large, W., & Yeager, S. G. (2009). The global climatology of an interannually varying air–sea flux data set. *Climate Dynamics*, *33*(2–3), 341–364. https://doi.org/10.1007/s00382-008-0441-3

Liang, J. H., McWilliams, J. C., Kurian, J., Colas, F., Wang, P., & Uchiyama, Y. (2012). Mesoscale variability in the northeastern tropical Pacific: Forcing mechanisms and eddy properties. *Journal of Geophysical Research: Oceans*, *117*(C7). https://doi.org/10.1029/2012jc008008

Mahadevan, A., Thomas, L. N., & Tandon, A. (2008). Comment on "Eddy/wind interactions stimulate extraordinary mid-ocean plankton blooms". *Science*, *320*(5875), 448. https://doi.org/10.1126/science.1152111

Martin, A. P., & Richards, K. J. (2001). Mechanisms for vertical nutrient transport within a North Atlantic mesoscale eddy. *Deep Sea Research Part II: Topical Studies in Oceanography*, *48*(4–5), 757–773. https://doi.org/10.1016/s0967-0645(00)00096-5

McGillicuddy, D. J., Ledwell, J. R., & Anderson, L. A. (2008). Response to Comment on "Eddy/wind interactions stimulate extraordinary mid-ocean plankton blooms". *Science*, *320*(5875), 448. https://doi.org/10.1126/science.1148974

McWilliams, J. C. (2016). Submesoscale currents in the ocean. *Proceedings of the Royal Society A: Mathematical, Physical and Engineering Sciences*, *472*(2189), 20160117. https://doi.org/10.1098/rspa.2016.0117

Morrison, A. K., Saenko, O. A., Hogg, A. M., & Spence, P. (2013). The role of vertical eddy flux in Southern Ocean heat uptake. *Geophysical Research Letters*, *40*(20), 5445–5450. https://doi.org/10.1002/2013GL057706

Neale, R. B., Chen, C. C., Gettelman, A., Lauritzen, P. H., Park, S., Williamson, D. L., et al. (2010). Description of the NCAR community atmosphere model (CAM 5.0). *NCAR Technical Note NCAR/TN-486+ STR*, *1*(1), 1–12.

Pond, S., & Pickard, G. L. (2013). *Introductory dynamical oceanography*. Gulf Professional Publishing.

Renault, L., McWilliams, J. C., & Masson, S. (2017). Satellite observations of imprint of oceanic current on wind stress by air-sea coupling. *Scientific Reports*, *7*(1), 1–7. https://doi.org/10.1038/s41598-017-17939-1

Risien, C. M., & Chelton, D. B. (2008). A global climatology of surface wind and wind stress fields from eight years of QuikSCAT scatterometer data. *Journal of Physical Oceanography*, *38*(11), 2379–2413. https://doi.org/10.1175/2008jpo3881.1

Saenko, O. A. (2015). Strong eddy compensation for the Gulf Stream heat transport. *Geophysical Research Letters*, *42*(24), 10739–10744. https://doi.org/10.1002/2015GL066111

Siegelman, L., Klein, P., Rivière, P., Thompson, A. F., Torres, H. S., Flexas, M., & Menemenlis, D. (2020). Enhanced upward heat transport at deep submesoscale ocean fronts. *Nature Geoscience*, *13*(1), 50–55. https://doi.org/10.1038/s41561-019-0489-1

Small, R. J., Bacmeister, J., Bailey, D., Baker, A., Bishop, S., Bryan, F., et al. (2014). A new synoptic scale resolving global climate simulation using the Community Earth System Model. *Journal of Advances in Modeling Earth Systems*, *6*(4), 1065–1094. https://doi.org/10.1002/2014ms000363

Smith, R. D., Jones, P., Briegleb, B., Bryan, F., Danabasoglu, G., Dennis, J., et al. (2010). *The Parallel Ocean Program (POP) reference manual* (Technical Report LAUR-10-01853). Los Alamos National Laboratory.

Stern, M. E. (1965). Interaction of a uniform wind stress with a geostrophic vortex. *Deep Sea Research and Oceanographic Abstracts*, *12*(3), 355–367. https://doi.org/10.1016/0011-7471(65)90007-0

Su, Z., Wang, J., Klein, P., Thompson, A. F., & Menemenlis, D. (2018). Ocean submesoscales as a key component of the global heat budget. *Nature Communications*, *9*(1), 1–8. https://doi.org/10.1038/s41467-018-02983-w

Wolfe, C. L., Cessi, P., McClean, J. L., & Maltrud, M. E. (2008). Vertical heat transport in eddying ocean models. *Geophysical Research Letters*, *35*(23). https://doi.org/10.1029/2008gl036138

Yang, P., Jing, Z., Sun, B., Wu, L., Qiu, B., Chang, P., & Ramachandran, S. (2021). On the upper-ocean vertical eddy heat transport in the Kuroshio extension. Part I: Variability and dynamics. *Journal of Physical Oceanography*, *51*(1), 229–246. https://doi.org/10.1175/jpo-d-20-0068.1